

Gold Nanoparticle Thin Film-Based Strain Sensors for Monitoring Human Pulse

Wei-Wun Jheng, Yu-Shun Su, Yun-Lien Hsieh, Yu-Jhan Lin, Shien-Der Tzeng, Chih-Wei Chang, Jenn-Ming Song, and Watson Kuo*



Cite This: *ACS Appl. Nano Mater.* 2021, 4, 1712–1718



Read Online

ACCESS |



Metrics & More



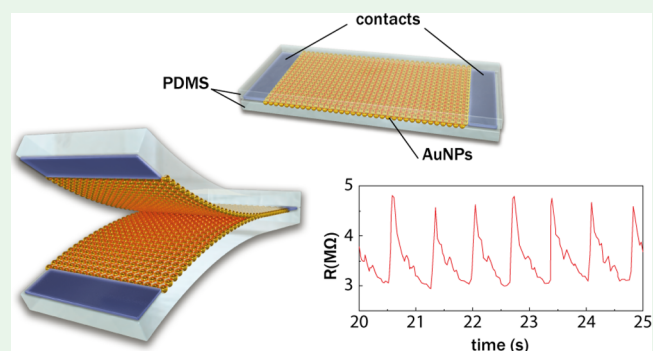
Article Recommendations



Supporting Information

ABSTRACT: A concise and economical way to build nanoparticle thin-film strain sensors of high gauge factors on a flexible polydimethylsiloxane substrate is developed. The gauge factors for resistance change and capacitance change are much larger than those of many other competing sensors. The small bulk modulus of the substrate provides the sensor a large responsivity for pressure with a frequency bandwidth of kHz. It can be used for tactile sensing that is capable of monitoring human pulse for pre-clinical diagnosis, by resolving minor structures such as peaks of diastolic pulse and before diastolic pulse in the waveforms.

KEYWORDS: nanoparticle, polydimethylsiloxane, piezoresistance, piezocapacitance, pressure sensing, human pulse monitoring, point-of-care



INTRODUCTION

Electronic skin, which can transduce pressure,^{1–4} temperature,⁵ and moisture⁶ signals into electrical ones, may find vast applications in robotics and medicine.⁷ In addition, the emerging mobile electronics revokes the development of pressure sensors because of the heavy reliance on a high-performance and low-cost component in human-machine interfaces.^{8–11} There is tremendous interest to develop microelectromechanical systems integrated with pressure sensors that allow for atmospheric or tactile applications with a very high resolution of sub-100 Pa. Except for a gentle touch that is in the kPa regime, such a resolution allows the barometric measurement to distinguish an altitude difference on the meter scale.¹² State-of-the-art tactile sensors could be made by taking advantage of piezoresistive, piezoelectric, and triboelectric effects. Piezoresistance devices,¹³ of which resistance changes according to stress (or strain), are good candidates for such a need. Regarding electrical measurement, three different types have been demonstrated in recent tactile sensors: resistive, capacitive, and field effect. The flexible field effect transistors made of organic¹⁴ or core–shell nanowires³ are suitable for the sensors; however, the complicated and expensive fabrication limits their usage for large area sensing. Some materials, such as Si and ZnO, have a large piezoelectric constant, allowing highly sensitive usage, but are limited by their small dynamic range due to their low flexibility.^{15–17} Recently, the emergent two-dimensional materials may be used

for a wider strain range but with a trade-off in lower sensitivity.¹⁸

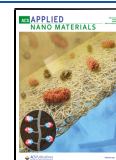
Much more trials were performed on composite materials made of conductor networks embedded in polymers, which can be engineered into sensors of resistive and capacitive types with a balance between sensitivity and dynamic range, together with performance and cost. Combined with soft and stretchable substrates, such as polydimethylsiloxane (PDMS) and Ecoflex silicone rubber, the strain sensors can be used for high-performance pressure sensing.¹⁹ In particular, flexible sensors can find much wide applications in industrial and medical fields since they are compatible with non-flat surfaces. Indeed, realistic applications including vibration detection, large human motion sensing, human pulse detections, and respiration monitoring have been demonstrated.^{19–21} These advances ensure that flexible sensors can be used for point-of-care testing.

Among the sensors made of composite materials, strain sensors made of metallic nanoparticles (NPs) have been demonstrated with great performance and are easy to build on various types of substrates.^{22–29} The large resistance change

Received: November 30, 2020

Accepted: January 14, 2021

Published: January 25, 2021



arises from the strain-sensitive hopping conduction in these NP films based on the conductance formula in the weak coupling regime at high temperatures,^{22,30}

$$G = G_0 e^{-\beta s} e^{-E_a/k_B T} \quad (1)$$

Here, s is the interparticle spacing, while β is a constant, typically between 9 and 13 nm⁻¹, depending on free space tunneling or molecule chain hopping as the interparticle conduction mechanism.³¹ E_a is the thermal activation energy that is related to the single particle Coulomb charging effect. At room temperature, E_a is usually smaller than the thermal energy $k_B T$ (~ 26 meV as temperature $T \approx 300$ K), so the factor $e^{-\beta s}$ becomes dominant in the conduction. As illustrated in Figure 1a, assuming that the organic molecules, which

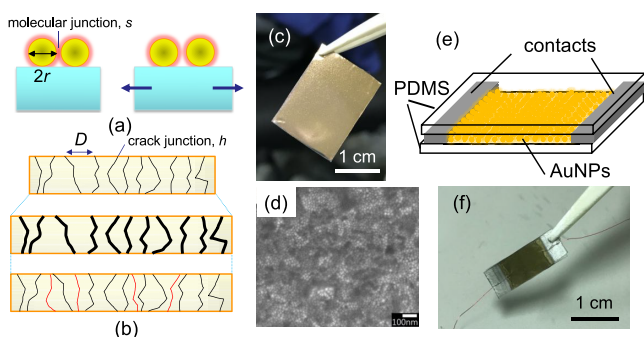


Figure 1. (a) Schematic of the molecular junctions formed between adjacent NPs. A tensile strain increases the interparticle distance spacing s . (b) Schematic of nanoscale crack junctions on the NP film. Either the crack gap, h , or crack number, N , would increase under a tensile strain. (c) Photograph of the AuNP film as-deposited on the PDMS substrate. (d) Electron micrograph of the deposited AuNP film. The scale bar is 100 nm. (e) Schematic drawing of the AuNP strain sensors. (f) Photograph of a strain sensor.

support the interparticle spacing s , are much more easily deformed than the NPs, we can estimate that the change of s under an isotropic expansion is given by $\Delta s = (2r + s)\epsilon$, in which r is the radius of NPs and ϵ denotes the strain. From eq 1, the relative resistance change as a function of ϵ reads

$$\Delta R/R_0 = e^{\beta \Delta s} - 1 = e^{g\epsilon} - 1 \quad (2)$$

in which R_0 is the device resistance in the absence of strain, $\Delta R = R - R_0$ is the resistance change, and $g = \beta(2r + s)$ is the gauge factor, which is typically used to quantify the performance of a strain sensor.

In addition to the strain-sensitive molecular junctions mentioned above, a recent work demonstrated mechanical sensing based on nanoscale crack junctions,³² which serves a good supplement to the large piezoresistive behavior in sensors based on NPs. As reported in our previous work³³ and other similar ones, cracks on the order of 10 nm do form during NP device fabrication and cyclic bending. Therefore, we cannot completely rule out the possible piezoresistive response due to nanoscale crack junctions. The concept of a crack sensory system is illustrated in Figure 1b. We may consider their contribution to the device gauge factor when the device resistance is dominated by the cracks using two scenarios: (i) crack gap increment and (ii) crack number increment. As illustrated and discussed in ref 32, the increment of the crack gap, h , under a tensile strain can be estimated by $\Delta h/h = \epsilon D/h$, in which D is the average distance between adjacent cracks and

$D \gg h$. Since the intercrack conduction in the NP assembly should also obey the tunneling law described by eq 1, the estimated gauge factor for this scenario is $g = \beta D$. In the other scenario, we presume solely the increment of the crack number, $\Delta N/N = \epsilon D/h$, without a change in h . Since the device resistance is linearly proportional to N , this increment should yield a gauge factor of $g = D/h$. For the polyimide substrate, we could estimate D to be 1 μm , so the g can be 10^4 in the incremented gap case and 10^2 in the incremented number case. A quantitative study of the device resistance and gauge factors should indicate which mechanism is more plausible.

In this work, we intend to develop tactile sensors based on the piezoresistive effect of the nanoparticle films. To simulate the mechanical property of human skin, which typically has a Young's modulus of $4\text{--}8 \times 10^5$ Pa, we choose PDMS, which typically has a Young's modulus of 10^6 Pa as the substrate material. PDMS is also widely used in biomedical applications due to it being optically clear, inert, and non-toxic. It has been demonstrated that the PDMS elastomer can be used as a base structure material of the tactile sensor. The deposition of a nanoparticle film is compatible with the PDMS material, and a simple and durable package scheme is developed. In addition to the expected high piezoresistive behavior, we also demonstrated high piezocapacitive results in similar devices with a higher resistance. Our findings may elucidate the mechanism of the capacitance change in the nanoparticle assembly as well as indicate the possibility of building sensors used in different electronic circuits by tuning fabrication parameters. The pressure responsivity of 3 kPa^{-1} and frequency bandwidth of 1 kHz allow us to sense the human pulse at the radial artery. The sensor is highly sensitive that it can resolve minor structures, such as peaks of diastolic pulse and before diastolic pulse in the waveforms. Though the nanoparticle is not a new face, the fabrication and packaging methods we introduced provide the superior behavior in the sensors having similar functions. The sensitivity of our sensors is one-order of magnitude higher than a very recent report on a NP-based pressure sensor, which is capable of detecting the atmospheric pressure change at an elevation of 10 m.¹² These achievements have widened the application with NP-based sensors in a new regime. Together with low-cost and easy-to-use, such a kind of sensor could find application in pre-clinical diagnosis.³⁴

EXPERIMENTAL METHODS

Gold nanoparticles (AuNPs) of 12 or 16 nm diameter were prepared by sodium citrate reduction of HAuCl₄ and were further modified with 3-mercaptopropionic acid (MPA).³⁵ The PDMS substrate (Gel-Pak PF-40/17-X8) surface was modified with 3-aminopropyltrimethoxysilane (APTMS) to assist the absorption of AuNPs. For this purpose, substrates were treated with atmospheric plasma at 0.5 torr with 15 min, followed by immersion in a solution containing APTMS for 9 h. AuNP colloidal solution (12 mL) was placed and spun at 10,000 rpm for 20 min in a 50 mL test tube for which a surface-modified PDMS substrate was attached to the inner surface. After being centrifuged and dried in air, a Au deposited film with a size of 20 mm \times 30 mm (Figure 1c) comprising 2–3 Au NP layers formed on the PDMS surface. We note that when the pH value of the colloidal solution is properly controlled, deposited AuNPs may form a closely packed thin film, in which the interparticle spacing was simply determined by the length of surface-modification molecule.³⁵ Figure 1d illustrates the scanning electron micrograph of a typical deposited film. The resistance of the as-fabricated device is related to the deposited NP layer number, which is controlled by the total NP

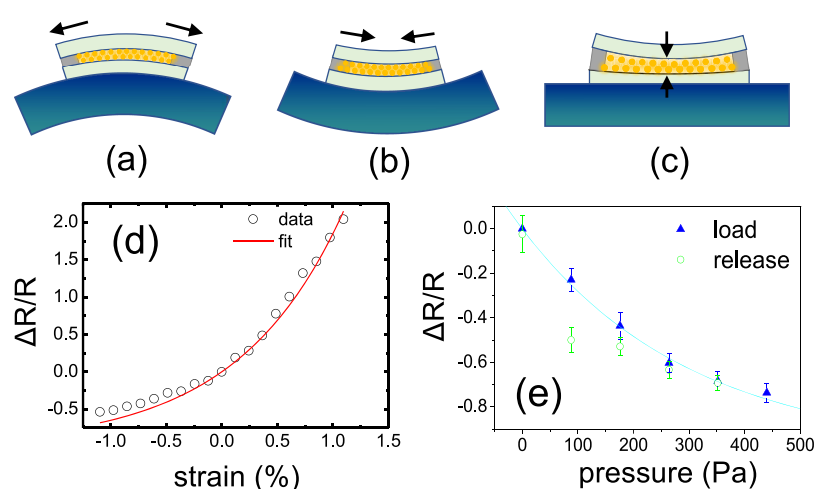


Figure 2. (a–c) Schematic diagrams for the device under the test of tensile strain (a), compression strain (b), and pressure (c). Both PDMS substrates are elongated in (a) and are compressed in (b). (d) Relative resistance change $\Delta R/R_0$ as a function of strain from -1.0 to 1.0% (symbols) of the same device corresponds well to the predicted formula (red curve) with $g \approx 104 \pm 1.08$. (e) Resistance change under a pressure up to 450 Pa. The procedures of pressure loading and releasing are shown. The curve presents the results with responsivity of 3.3 kPa^{-1} .

amount in the solution. The Au NP-coated PDMS substrate was then dissected into two $20 \text{ mm} \times 5 \text{ mm}$ strips. To assemble the device, these two strips were attached to each other with the Au film coated faces. Commercial Ag paste was used to package the device and conduct the signal to Cu wires. Since the process was done manually, we cannot exclude the possible strain that resulted from the substrate binding process. Indeed, even a tiny strain could cause a large resistance change because the gauge factor of the nanoparticle device is great. Unlike the fabrication scheme proposed by others, our device did not undergo a post-annealing process to prevent any degrading of the surface-modified molecules. Figure 1e,f shows the schematic and photograph of the assembled strain sensor, respectively.

To have a step-by-step change of the strain, the sensor substrate was attached onto a printed circuit board, which could be bended on a homemade test platform.³³ The applied strain could range between -1.0 and 1.0% with $<0.1\%$ accuracy, which was calibrated by a commercial metal foil strain gauge. The resistance of the sensor is inferred from the current–voltage measurement with a typical bias voltage of 0.1 V . Capacitance measurement is done using a capacitance bridge (Andeen-Hagerling 2500A) with a resolution of 0.5 aF . The detection signal is 0.75 V at a frequency of 1 kHz . To study the response under the pressure, small weights were used to exert a uniform force onto the sensors. The frequency response of the sensor was done using a loud speaker. Two methods were applied to introduce the vibrations to the device: Devices were directly attached to the speaker diaphragm or were suspended allowing single-point contact to the diaphragm. To produce the single frequency vibrations, the speaker is driven by sinusoidal voltage signals from 10 Hz to 2 kHz . The detail of the setup can be found in Supporting Information, Section II.

RESULTS AND DISCUSSION

Pressure Responsivity. The tensile and compressive strains were applied using two bending schemes illustrated in Figures 2a,b. Because of the low bulk modulus of the PDMS substrate (a few MPa), the device can be used as a pressure sensor. Figure 2c schematically displays the deformation of the device under a pressure. It can be expected that the device resistance will drop in Figure 2b,c due to the reduction in interparticle spacing. Figure 2d shows the sensor response $\Delta R/R_0$ as a function of strain ϵ under the stepwise change of strain. In the small strain region, from -1.0 to 1.0% , we found that $\Delta R/R_0$ follows the prediction of eq 2 with a gauge factor $g = 104$. Our previous work has shown a tunneling decay constant

β of 11.8 nm^{-1} . The expected value is roughly 150 by using the AuNP radius $r = 6 \text{ nm}$ and a typical s of 1 nm for MPA-modified molecular junctions. It is also compatible with the incremented number scenario for crack junctions when $D = 1 \mu\text{m}$ and $h = 10 \text{ nm}$. The resistance was found to be reduced if a pressure is loaded to the device surface as illustrated in Figure 2e. The quality of a pressure gauge can be determined by the responsivity, which is defined as

$$R_p = \frac{\Delta R/R}{\Delta P} \quad (3)$$

when the applied pressure ΔP is very small. The curve in Figure 2b is the function $\Delta R/R = e^{-R_p P} - 1$ with $R_p = 3.3 \text{ kPa}^{-1}$. Although the well-controlled tests were performed in the small strain and pressure range, the devices can endure a big strain and recover quickly. Due to the large gauge factor, a greater elongation deformation can result in the sensor an open circuit. In a simple trial, a gentle touch of the device using finger, which is on the $10\text{--}20 \text{ kPa}$ range, can reduce the resistance of the device for more than 1 order of magnitude.

According to previous works done by us and others, enlarged NPs will improve the gauge factors linearly, which can be easily seen from the theoretical prediction in eq 2. On average, our device made of 16 nm NPs has a greater gauge factor than that made of 12 nm NPs. However, the film assembled with larger-size NPs typically has much more defects and the device resistances are generally greater and with a bigger variation. Regarding the realistic applications, a good choice to balance the performance and sample yield for our deposition method will be a size of 12 nm . Another possible factor, which does not appear in theory, is the (as-fabricated) device resistance, which can be reduced by the deposited NP layer. A general result is that the intermediate resistance, roughly $3\text{--}6 \text{ M}\Omega$, displays the best gauge factor. However, the total layer number of the thin film does not have a clear impact on the result. The details about how the gauge factor depends on the device resistance and NP layer can be found in Supporting Information, Section III. Since the parameters were not varied large enough in the current results, we would leave these issues for future studies.

Capacitance Gauge Factor. From Abele's formula, we can estimate the capacitance of a molecular junction as

$$C = 4\pi\kappa\epsilon_0(s + r)r/s \quad (4)$$

Here, κ is the medium dielectric constant. The change of C increases the charging energy, which is the effective activation energy for single charge tunneling in the molecular junction. As such, it may hinder the charge transport. However, the charging energy is smaller than the room-temperature thermal energy, so the resistance change due to the C change is negligible. An alternative way to verify change of C can be done by capacitance measurement. Abele's formula predicts that the capacitance change is $\Delta C/C \sim -\Delta s/s \sim (2r/s)\epsilon$, and a gauge factor for C change $g_c = 2r/s$. According to our device parameters $r = 6$ nm and $s = 1$ nm, g_c originating from molecular junctions is roughly 10. Similar to Abele's formula, the capacitance associated with each crack junction should scale with $1/h$, and the total capacitance due to N cracks scales as $C \propto 1/hN$. Either incremented gap scenario, $\Delta h/h = \epsilon D/h$, or incremented number scenario, $\Delta N/N = \epsilon D/h$, yields a similar gauge factor in C change with $g_c = D/h = 100$, which could be much greater than that for molecular junctions.

As illustrated in Figure 3a,b, we measured the capacitance change of a typical sample (sample 1) with $C \approx 0.5$ nF and $R \approx$

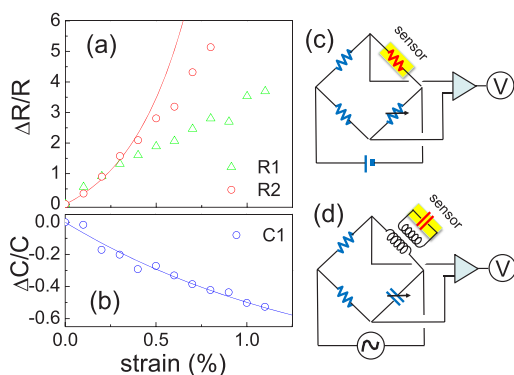


Figure 3. (a) Resistance change of the sensor with high resistance (100 M Ω , R1 data) and lower resistance (40 M Ω , R2 data) samples. The curve presents a gauge factor of 300. (b) Capacitance change of the high resistance sensor. The gauge factor for the C change is 69. (c) Standard bridge circuit for resistance measurement. (d) Bridge circuit for monitoring a capacitance coupled inductively. Elements in blue colors are standard resistances and capacitance.

100 M Ω . The capacitance bridge provides simultaneously the readings of C and loss, which can be inferred as device resistance R . At strain $\epsilon = 1.0\%$, the capacitance reduces to 0.25 nF while R increases to 1.1 G Ω . The C data can be nicely fit to a result $\Delta C/C = e^{-g_c\epsilon} - 1$ with $g_c = 69$. Similar to the gauge factor for R , the g_c value is much bigger than the one derived from Abele's formula but smaller than what the crack mechanism suggests. The resistance change for sample 1 does not follow well with the prediction of an exponential increment, probably due to the inaccurate reading of a high resistance ~ 1 G Ω . For another device whose R is 40 M Ω , the resistance reading follows the exponential behavior better below the resistance of 160 M Ω . However, the measurement on capacitance change becomes unstable with this low loss sample. To summarize gauge factors for R and C change in our devices, we could confirm that both molecular junctions and

crack junctions contribute to the strain sensitivity, while the latter one should work in the incremented number scenario.

Our results indicate that both the piezoresistive and piezocapacitive behaviors can be displayed in these metallic NP sensors with considerable large gauge factors. In comparison to the most general bridge circuit applied for a piezoresistive sensor shown in Figure 3c, an ac signal is generally used to monitor a capacitance, allowing the sensing circuit and monitoring circuit possibly coupled inductively as shown in Figure 3d. The benefit arises due to the noncontact between the circuits, thus widening the potential applications for a capacitive sensor for sensing the deformation and/or the load in moving structures, e.g., a rotor. Table 1 lists the gauge

Table 1. Summary of Important Reported Electronic Pressure Sensors Based on Nanoparticles

NP material	substrate	gauge factor	strain range	pressure sensitivity (per kPa)	ref
Au	PDMS	>100	1%	3.3	our work
Au	variety, e.g., Mylar	50–250	<1%	N/A	Segev-Bar et al. ³⁶
Ag	PDMS	2	20%	0.35	Lee et al. ³⁷
Cr	PET	>100	0.4%	N/A	Zhen et al. ³⁸
SiO ₂	PDMS	N/A	N/A	0.44	Kim et al. ³⁹
Pd	PET	30	<1%	0.13	Chen et al. ¹²

factors and pressure sensitivities that have been reported very recently in NP sensors. Among the collected data, our pressure sensors outperform others for the usage in the small strain range.

Frequency Response. Under the driving of the diaphragm, the current-biased sensors generate sinusoidal voltage signals as illustrated in Figure 4a. The ac voltage component, which is in accordance with the driving voltage, originates from the piezoresistive change. However, if the bias current is turned off, there is a small modulation of the voltage,

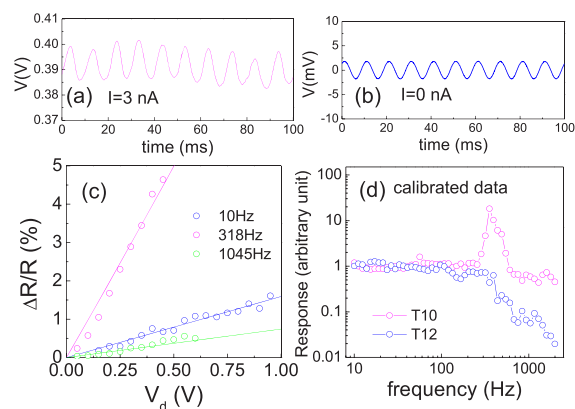


Figure 4. (a, b) Device voltage as a function of time when driven by a 100 Hz vibration. The bias current is 3 nA (a) and 0 nA (b). At zero bias, the voltage majorly contributed from the Faraday induction. The resistance change was determined by subtracting the induction background of the voltage signals. (c) Relative resistance change of the device under the vibration driving at 10, 318, and 1045 Hz. The resistance change linearly depends on the driving voltage V_d . (d) Calibrated frequency response of the tactile sensors T10 and T12. In both cases, they show the bandwidth of about 1 kHz.

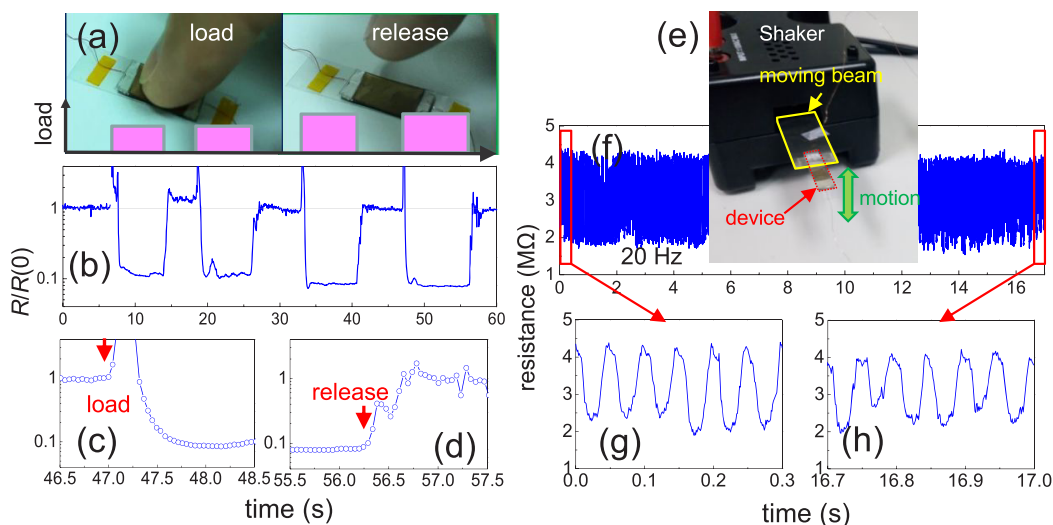


Figure 5. (a) Test of device resistance change under a gentle touch. (b) Relative change $R/R(0)$ in device resistance in the log scale. The touches reduce the relative resistance to 0.13 or 0.07 under different loads. (c, d) Zoomed-in images showing the transient behavior of the resistance change. Within 1 s, the resistance may respond to a stable value. (e) Multicycle test was done using a shaker oscillating at a frequency of 20 Hz. (f) Total test time in this scan is 17 s. The device resistance showed a similar waveform in the very beginning (g) and at the end of the test (h).

which should be attributed to the induction due to the mechanical motions. As shown in Figure 4b, the induction voltage signal is about 5 mV peak-to-peak at 100 Hz and increases linearly with driving frequency. Therefore, to extract the contribution from the piezoresistive effect, we subtract the unbiased voltage from the biased data and determine the resistance change amplitude. The resistance change linearly increases as the driving voltage amplitude as shown in Figure 4c. From the slope of the plot, one can determine the response of the sensor and speaker under V_d driving. Provided the speaker typical has a large bandwidth from 20 Hz to 20 kHz, the data may provide the response of the sensors in this frequency range. The results for attached (sample T10) and point contacted (sample T12) are shown in Figure 4d. To remove any frequency response from the loud speaker, we performed a calibration procedure as described in the Supporting Information.

Response Time and Durability. To demonstrate the response time for our sensor, we performed a simple test by monitoring the resistance when the device experienced a gentle finger touch as shown in Figure 5a. Due to the high sensitivity to pressure, the relative resistance reduces to 0.13 or 0.07 under the lighter or stronger pressing. The data presented in Figure 5b clearly shows that when experiencing such a great change over one order of magnitude, the device resistance can get restored to its initial value. Moreover, in the vicinity of applying and releasing the load, a transient time in resistance change is well below 1 s as what can be judged in Figure 5c,d. We also note that if a long holding time during testing was maintained, the resistance may exhibit a drift with a characteristic time of about 100 s and at an initial drift rate of about $10^{-4}/s$ under a small strain or load. It could originate from the slow redistribution of the strain on the PDMS substrate. Generally, when the device is totally released from the load for much longer than the characteristic time, the device resistance may be restored.

To test the long-time repeatability and durability, we conducted continuous cycling of the device bending at 20 Hz using a shaker. One side of the device was attached to the shaking beam, while the other side was free to move as

illustrated in Figure 5e. In the data shown in Figure 5f, similar behavior remains over 340 cycles, in one of which the device resistance changes from 2 to 4 M Ω . Figure 5g,h shows the time scans of the device resistance at the beginning and at the end of this test, respectively. It is worth noting that such a kind of high frequency test was typically conducted for roughly 30 min with more than 30,000 cycles. Our devices did not show remarkable degrading after such intensive tests.

Human Pulse Measurement. The pressure responsivity and frequency bandwidth of the sensors are possible to be used in monitoring human activities such as pulse. As shown in Figure 6a, the sensor is simply attached to the wrist without

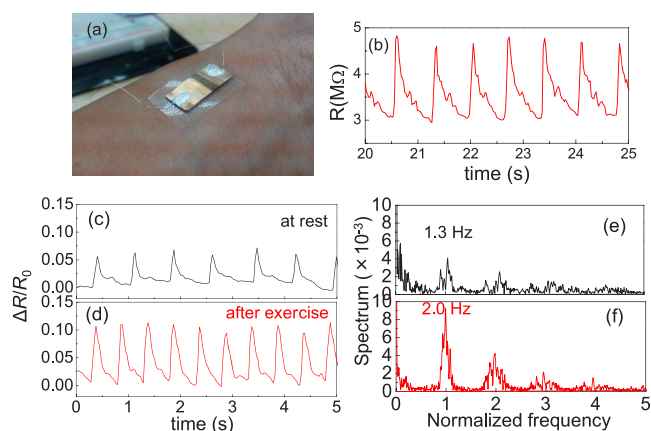


Figure 6. (a) Sensor was attached to the wrist of subject for detecting human pulses. (b) Real-time scan of the sensor resistance as a function of time. The single pulse may produce a resistance change of about 50%. Such a large change allows us to resolve small structures, such as peaks of diastolic pulse and before diastolic pulse. (c, d) Pulse waveforms taken when the subject was at rest (c) and after 10 min of intensive exercise (d). After-exercise waveform displays a greater pulse rate and pulse height, showing an intense heartbeat. (e, f) Fourier spectrum of the waveforms in (c) and (d) scaled by their fundamental frequencies, 1.3 and 2.0 Hz, respectively. The at-rest spectrum (e) presents split peaks while the after-exercise one (f) shows single and sharp peaks.

any load. The device can transduce tiny vibrations on the skin surface to large variations in resistance as shown in Figure 6b. It may produce a resistance change of 50% and small structures, such as dicrotic pulse and before dicrotic pulse, can be resolved with our sensors. Moreover, we note that the pulse waveforms taken when the subject was after intensive exercise (Figure 6d) not only display a greater pulse rate and amplitude than that at rest (Figure 6c) but also clearly show difference in their Fourier spectrum as illustrated in Figure 6e,f. Instead of showing split peaks as the at-rest one, the after-exercise spectrum presents single and sharp peaks although similar pulse measurements have been demonstrated using different kinds of strain/pressure sensors but they can only transduce into very crude pulse shape. Our results, which can provide very accurate waveform, may provide better information for pre-clinical diagnosis. Currently, medical sensors for point-of-care are under fast and vast development for rapid and low-cost analysis of various targets. Our devices, which only requires hand-held electrical monitoring equipment, can be easily combined with those for sensing oxygen,⁴⁰ glucose,⁴¹ uric acid,⁴² albumin,⁴³ lipase,⁴⁴ etc.

CONCLUSIONS

In summary, we built nanoparticle thin-film strain sensors on a flexible and stretchable PDMS substrate and demonstrated piezoresistance and piezocapacitance. The gauge factors for the R change are typically larger than 100, while for the C -change, they are ~ 60 . It is found that a device with higher resistance is more suitable for capacitance monitoring. The soft substrate PDMS allows us to use the sensors for small pressure measurement with a responsivity of 3.3 kPa^{-1} , which is capable in the usage for tactile detection. The frequency response of about a few kHz is limited by the mechanical loss of the substrate. Nevertheless, the bandwidth allows us to monitor the human pulse signals when the sensor is attached to the wrist. The sensors are capable of providing very accurate waveforms for pre-clinical diagnosis, such as dicrotic pulse and before dicrotic pulse, and distinguishing the waveforms taken at rest and after the exercise by Fourier transform. Currently, medical sensors for point-of-care are under fast and vast development for rapid and low-cost analysis of various targets. Our devices, which only require hand-held electrical monitoring equipment, can be easily integrated in the sensory system for such a need.

ASSOCIATED CONTENT

Supporting Information

The Supporting Information is available free of charge at <https://pubs.acs.org/doi/10.1021/acsnm.0c03167>.

Device packaging method, (2) experimental setup for frequency response and calibration procedure, (3) comparison of the NP deposition layer and as-fabricated resistance, (4) comparison of devices made on polyimide and PDMS substrates, and (5) justification of resistance change and Faraday induction from the data (PDF)

AUTHOR INFORMATION

Corresponding Author

Watson Kuo – Department of Physics, National Chung Hsing University, Taichung 402, Taiwan; orcid.org/0000-0002-9344-6778; Email: wkuo@phys.nchu.edu.tw

Authors

Wei-Wun Jheng – Department of Physics, National Chung Hsing University, Taichung 402, Taiwan

Yu-Shun Su – Department of Materials Science and Engineering, National Chung Hsing University, Taichung 402, Taiwan

Yun-Lien Hsieh – Department of Physics, National Chung Hsing University, Taichung 402, Taiwan

Yu-Jhan Lin – Center for Condensed Matter Sciences, National Taiwan University, Taipei 106, Taiwan

Shien-Der Tzeng – Department of Physics, National Dong Hwa University, Hualien 974, Taiwan

Chih-Wei Chang – Center for Condensed Matter Sciences, National Taiwan University, Taipei 106, Taiwan; orcid.org/0000-0003-0956-3179

Jenn-Ming Song – Department of Materials Science and Engineering, National Chung Hsing University, Taichung 402, Taiwan

Complete contact information is available at:

<https://pubs.acs.org/10.1021/acsnm.0c03167>

Notes

The authors declare no competing financial interest.

ACKNOWLEDGMENTS

The authors are grateful to C. S. Wu and C. C. Wu for fruitful discussions. This work was financially supported by the Ministry of Science and Technology, Taiwan under Grant No. MOST 109-2112-M-005-001.

REFERENCES

- (1) Someya, T.; Sekitani, T.; Iba, S.; Kato, Y.; Kawaguchi, H.; Sakurai, T. A large-area, flexible pressure sensor matrix with organic field-effect transistors for artificial skin applications. *Proc. Natl. Acad. Sci. U. S. A.* **2004**, *101*, 9966–9970.
- (2) Mannsfeld, S. C. B.; Tee, B. C. K.; Stoltenberg, R. M.; Chen, C. V. H. H.; Barman, S.; Muir, B. V. O.; Sokolov, A. N.; Reese, C.; Bao, Z. Highly sensitive flexible pressure sensors with microstructured rubber dielectric layers. *Nat. Mater.* **2010**, *9*, 859–864.
- (3) Takei, K.; Takahashi, T.; Ho, J. C.; Ko, H.; Gillies, A. G.; Leu, P. W.; Fearing, R. S.; Javey, A. Nanowire active-matrix circuitry for low-voltage macroscale artificial skin. *Nat. Mater.* **2010**, *9*, 821–826.
- (4) Hu, W.; Niu, X.; Zhao, R.; Pei, Q. Elastomeric transparent capacitive sensors based on an interpenetrating composite of silver nanowires and polyurethane. *Appl. Phys. Lett.* **2013**, *102*, No. 083303.
- (5) Jeon, J.; Lee, H.-B.-R.; Bao, Z. Flexible Wireless Temperature Sensors Based on Ni Microparticle-Filled Binary Polymer Composites. *Adv. Mater.* **2013**, *25*, 850–855.
- (6) Feng, J.; Peng, L.; Wu, C.; Sun, X.; Hu, S.; Lin, C.; Dai, J.; Yang, J.; Xie, Y. Giant Moisture Responsiveness of VS₂ Ultrathin Nanosheets for Novel Touchless Positioning Interface. *Adv. Mater.* **2012**, *24*, 1969–1974.
- (7) Hammock, M. L.; Chortos, A.; Tee, B. C.-K.; Tok, J. B.-H.; Bao, Z. 25th Anniversary Article: The Evolution of Electronic Skin (E-Skin): A Brief History, Design Considerations, and Recent Progress. *Adv. Mater.* **2013**, *25*, 5997–6038.
- (8) Lipomi, D. J.; Vosgueritchian, M.; Tee, B. C. K.; Hellstrom, S. L.; Lee, J. A.; Fox, C. H.; Bao, Z. Skin-like pressure and strain sensors based on transparent elastic films of carbon nanotubes. *Nat. Nanotechnol.* **2011**, *6*, 788–792.
- (9) Yamada, T.; Hayamizu, Y.; Yamamoto, Y.; Yomogida, Y.; Izadi-Najafabadi, A.; Futaba, D. N.; Hata, K. A stretchable carbon nanotube strain sensor for human-motion detection. *Nat. Nanotechnol.* **2011**, *6*, 296–301.

- (10) Pang, C.; Lee, G.-Y.; Kim, T.-i.; Kim, S. M.; Kim, H. N.; Ahn, S.-H.; Suh, K.-Y. A flexible and highly sensitive strain-gauge sensor using reversible interlocking of nanofibres. *Nat. Mater.* **2012**, *11*, 795–801.
- (11) Ying, M.; Bonifas, A. P.; Lu, N.; Su, Y.; Li, R.; Cheng, H.; Ameen, A.; Huang, Y.; Rogers, J. A. Silicon nanomembranes for fingertip electronics. *Nanotechnology* **2012**, *23*, 344004.
- (12) Chen, M.; Luo, W.; Xu, Z.; Zhang, X.; Xie, B.; Wang, G.; Han, M. An ultrahigh resolution pressure sensor based on percolative metal nanoparticle arrays. *Nat. Commun.* **2019**, *10*, 4024.
- (13) Bridgman, P. The effect of tension on the transverse and longitudinal resistance of metals. In *Proceedings of the American Academy of Arts and Sciences*; JSTOR, 1925, pp 423–449.
- (14) Kaltenbrunner, M.; Sekitani, T.; Reeder, J.; Yokota, T.; Kuribara, K.; Tokuhara, T.; Drack, M.; Schwödiauer, R.; Graz, I.; Bauer-Gogonea, S.; Bauer, S.; Someya, T. An ultra-lightweight design for imperceptible plastic electronics. *Nature* **2013**, *499*, 458–463.
- (15) He, R.; Yang, P. Giant piezoresistance effect in silicon nanowires. *Nat. Nanotechnol.* **2006**, *1*, 42–46.
- (16) Wu, W.; Wen, X.; Wang, Z. L. Taxel-Addressable Matrix of Vertical-Nanowire Piezotronic Transistors for Active and Adaptive Tactile Imaging. *Science* **2013**, *340*, 952–957.
- (17) Cha, S. N.; Seo, J.-S.; Kim, S. M.; Kim, H. J.; Park, Y. J.; Kim, S.-W.; Kim, J. M. Sound-Driven Piezoelectric Nanowire-Based Nanogenerators. *Adv. Mater.* **2010**, *22*, 4726–4730.
- (18) Park, M.; Park, Y. J.; Chen, X.; Park, Y.-K.; Kim, M.-S.; Ahn, J.-H. MoS₂-Based Tactile Sensor for Electronic Skin Applications. *Adv. Mater.* **2016**, *28*, 2556–2562.
- (19) Schwartz, G.; Tee, B. C. K.; Mei, J.; Appleton, A. L.; Kim, D. H.; Wang, H.; Bao, Z. Flexible polymer transistors with high pressure sensitivity for application in electronic skin and health monitoring. *Nat. Commun.* **2013**, *4*, 1859.
- (20) Yi, L.; Jiao, W.; Wu, K.; Qian, L.; Yu, X.; Xia, Q.; Mao, K.; Yuan, S.; Wang, S.; Jiang, Y. Nanoparticle monolayer-based flexible strain gauge with ultrafast dynamic response for acoustic vibration detection. *Nano Res.* **2015**, *8*, 2978–2987.
- (21) Tao, L.-Q.; Wang, D.-Y.; Tian, H.; Ju, Z.-Y.; Liu, Y.; Pang, Y.; Chen, Y.-Q.; Yang, Y.; Ren, T.-L. Self-adapted and tunable graphene strain sensors for detecting both subtle and large human motions. *Nanoscale* **2017**, *9*, 8266–8273.
- (22) Herrmann, J.; Müller, K.-H.; Reda, T.; Baxter, G. R.; Raguse, B.; de Groot, G. J. J. B.; Chai, R.; Roberts, M.; Wieczorek, L. Nanoparticle films as sensitive strain gauges. *Appl. Phys. Lett.* **2007**, *91*, 183105.
- (23) Farcau, C.; Sangeetha, N. M.; Moreira, H.; Viallet, B.; Grisolia, J.; Ciuculescu-Pradines, D.; Ressler, L. High-Sensitivity Strain Gauge Based on a Single Wire of Gold Nanoparticles Fabricated by Stop-and-Go Convective Self-Assembly. *ACS Nano* **2011**, *5*, 7137–7143.
- (24) Yin, J.; Hu, P.; Luo, J.; Wang, L.; Cohen, M. F.; Zhong, C.-J. Molecularly Mediated Thin Film Assembly of Nanoparticles on Flexible Devices: Electrical Conductivity versus Device Strains in Different Gas/Vapor Environment. *ACS Nano* **2011**, *5*, 6516–6526.
- (25) Alvares, D.; Wieczorek, L.; Raguse, B.; Ladouceur, F.; Lovell, N. Nanoparticle films as biomimetic tactile sensors. *Procedia Eng.* **2011**, *25*, 1349–1352.
- (26) Vossmeier, T.; Stolte, C.; Ijeh, M.; Kornowski, A.; Weller, H. Networked Gold-Nanoparticle Coatings on Polyethylene: Charge Transport and Strain Sensitivity. *Adv. Funct. Mater.* **2008**, *18*, 1611–1616.
- (27) Tanner, J. L.; Mousadakos, D.; Giannakopoulos, K.; Skotadis, E.; Tsoukalas, D. High strain sensitivity controlled by the surface density of platinum nanoparticles. *Nanotechnology* **2012**, *23*, 285501.
- (28) Farcau, C.; Moreira, H.; Viallet, B.; Grisolia, J.; Ciuculescu-Pradines, D.; Amiens, C.; Ressler, L. Monolayered Wires of Gold Colloidal Nanoparticles for High-Sensitivity Strain Sensing. *J. Phys. Chem. C* **2011**, *115*, 14494–14499.
- (29) Segev-Bar, M.; Haick, H. Flexible Sensors Based on Nanoparticles. *ACS Nano* **2013**, *7*, 8366–8378.
- (30) Huth, M. Granular metals: From electronic correlations to strain-sensing applications. *J. Appl. Phys.* **2010**, *107*, 113709.
- (31) Slowinski, K.; Chamberlain, R. V.; Miller, C. J.; Majda, M. Through-bond and chain-to-chain coupling. Two pathways in electron tunneling through liquid alkanethiol monolayers on mercury electrodes. *J. Am. Chem. Soc.* **1997**, *119*, 11910–11919.
- (32) Kang, D.; Pikhitsa, P. V.; Choi, Y. W.; Lee, C.; Shin, S. S.; Piao, L.; Park, B.; Suh, K.-Y.; Kim, T.-i.; Choi, M. Ultrasensitive mechanical crack-based sensor inspired by the spider sensory system. *Nature* **2014**, *516*, 222–226.
- (33) Jiang, C.-W.; Ni, I. C.; Tzeng, S.-D.; Kuo, W. Nearly isotropic piezoresistive response due to charge detour conduction in nanoparticle thin films. *Sci. Rep.* **2015**, *5*, 11939.
- (34) Gubala, V.; Harris, L. F.; Ricco, A. J.; Tan, M. X.; Williams, D. E. Point of Care Diagnostics: Status and Future. *Anal. Chem.* **2012**, *84*, 487–515.
- (35) Ni, I. C.; Yang, S. C.; Jiang, C. W.; Luo, C. S.; Kuo, W.; Lin, K. J.; Tzeng, S. D. Formation Mechanism, Patterning, and Physical Properties of Gold-Nanoparticle Films Assembled by an Interaction-Controlled Centrifugal Method. *J. Phys. Chem. C* **2012**, *116*, 8095–8101.
- (36) Segev-Bar, M.; Landman, A.; Nir-Shapira, M.; Shuster, G.; Haick, H. Tunable Touch Sensor and Combined Sensing Platform: Toward Nanoparticle-based Electronic Skin. *ACS Appl. Mater. Interfaces* **2013**, *5*, 5531–5541.
- (37) Lee, J.; Kim, S.; Lee, J.; Yang, D.; Park, B. C.; Ryu, S.; Park, I. A stretchable strain sensor based on a metal nanoparticle thin film for human motion detection. *Nanoscale* **2014**, *6*, 11932–11939.
- (38) Zheng, M.; Li, W.; Xu, M.; Xu, N.; Chen, P.; Han, M.; Xie, B. Strain sensors based on chromium nanoparticle arrays. *Nanoscale* **2014**, *6*, 3930–3933.
- (39) Kim, H.; Kim, G.; Kim, T.; Lee, S.; Kang, D.; Hwang, M.-S.; Chae, Y.; Kang, S.; Lee, H.; Park, H.-G.; Shim, W. Transparent, Flexible, Conformal Capacitive Pressure Sensors with Nanoparticles. *Small* **2018**, *14*, 1703432.
- (40) Shen, L.; Ratterman, M.; Klotzkin, D.; Papautsky, I. Use of a Low-Cost CMOS Detector and Cross-Polarization Signal Isolation for Oxygen Sensing. *IEEE Sens. J.* **2011**, *11*, 1359–1360.
- (41) Taguchi, M.; Ptitsyn, A.; McLamore, E. S.; Claussen, J. C. Nanomaterial-mediated biosensors for monitoring glucose. *J. Diabetes Sci. Technol.* **2014**, *8*, 403–411.
- (42) Liu, X.; Lin, P.; Yan, X.; Kang, Z.; Zhao, Y.; Lei, Y.; Li, C.; Du, H.; Zhang, Y. Enzyme-coated single ZnO nanowire FET biosensor for detection of uric acid. *Sensors and Actuators B: Chemical* **2013**, *176*, 22–27.
- (43) Reja, S. I.; Khan, I. A.; Bhalla, V.; Kumar, M. A TICT based NIR-fluorescent probe for human serum albumin: a pre-clinical diagnosis in blood serum. *Chem. Commun.* **2016**, *52*, 1182–1185.
- (44) Middya, S.; Bhattacharjee, M.; Mandal, N.; Bandyopadhyay, D. RGO-Paper Sensor for Point-of-Care Detection of Lipase in Blood Serum. *IEEE Sensors Letters* **2018**, *2*, 1–4.